Research Article | Vol. 27, No. 21 / 14 October 2019 / Optics Express 30931
Optics EXPRESS

Ultra-thin transmissive crystalline silicon high-contrast grating metasurfaces

He Li,[1,2] Daan P. Stellinga,[3] Yunmin Qiu,[1,2] Qian Sun,[1,2] Bo Chen,[1,2] Haowen Liang,[1,2,*] Thomas F. Krauss,[3,1] and Juntao Li[1,2]

[1]State Key Laboratory of Optoelectronic Materials and Technologies, Sun Yat-Sen University, Guangzhou, 510275, China
[2]School of Physics, Sun Yat-Sen University, Guangzhou, 510275, China
[3]Department of Physics, University of York, York, YO10 5DD, UK
[*]lianghw26@mail.sysu.edu.cn

Abstract: Dielectric metasurfaces made from crystalline silicon, titanium dioxide, gallium nitride and silicon nitride have developed rapidly for applications in the visible wavelength regime. High performance metasurfaces typically require the realisation of subwavelength, high aspect ratio nanostructures, the fabrication of which can be challenging. Here, we propose and demonstrate the operation of high performance metasurfaces in ultra-thin (100 nm) crystalline silicon at the wavelength of 532 nm. Using optical beam analysis, we discuss fabrication complexity and show that our approach is more fabrication-tolerant than the nanofin approach, which has so far produced the highest performance metasurfaces, but may be difficult to manufacture, especially when using nanoimprint lithography.

1. Introduction

Controlling and shaping light beams at will is one of the major goals of photonics research. Over the years, various demonstrations of ordinary and extraordinary optical phenomena have been enabled by structuring artificial materials at the sub-wavelength scale [1–4]. More recently, the concept of the metasurface emerged [5], which consists of thin resonant elements that can modulate optical wavefronts by manipulating the phase [6], amplitude [7] or polarization of light [8]. These artificial optical structures were initially demonstrated in the form of metallic metasurfaces [6,9–16]. However, metallic structures have limited efficiency in the visible regime due to ohmic loss, which particularly restricts their use in transmission. This limitation has now focused the metasurface research effort onto dielectric materials.

Such dielectric metasurfaces can be categorized according to the nature of the material into "high index" semiconductors such as silicon and "low index" oxides and nitrides [17–31]. The issue with the high index semiconductors is their absorption in the visible regime, but it has recently been shown that this loss can be mitigated by using advanced designs of crystalline silicon (c-Si) metasurfaces on transparent substrates, with efficiencies close to those obtained with dielectric materials now having been demonstrated, even at 532 nm wavelength [32–37].

Here we propose to use ultra-thin c-Si of 100 nm thickness, which is several times thinner than the silicon used previously (e.g. 380 nm [36] to 500 nm [37]). Our unit cell consists of a high-contrast grating (HCG), which is able to provide full 2π phase control for circular polarized incident beams. A high efficiency orbital angular momentum (OAM) generator is then designed and fabricated to demonstrate the capability. Finally, we discuss fabrication issues and show that using thinner material markedly improves fabrication tolerance, especially in view of manufacturing by nanoimprint lithography.

#374550 https://doi.org/10.1364/OE.27.030931
Journal © 2019 Received 2 Aug 2019; revised 20 Sep 2019; accepted 22 Sep 2019; published 10 Oct 2019

Optics EXPRESS

2. Design and fabrication

It is well established that the HCG approach allows full 2π phase control [19,20,35,36]. In order to facilitate the detailed design, we then used finite difference time domain (FDTD) calculations to generate the phase map of the HCG by varying its width and periodicity for a wavelength of 532 nm. By varying the thickness from 80 nm to 120 nm, the phase difference between TE-polarized and the TM-polarized incident light can be controlled between 1.44π to 0.96π, with a value of 0.99π being obtained for a thickness of 100 nm (Fig. 1 shows the simulated phase maps of TE- and TM-polarized light under different geometrical parameters). Therefore, we chose 100 nm to create a half-wave plate. Regarding the HCG period, we found that an

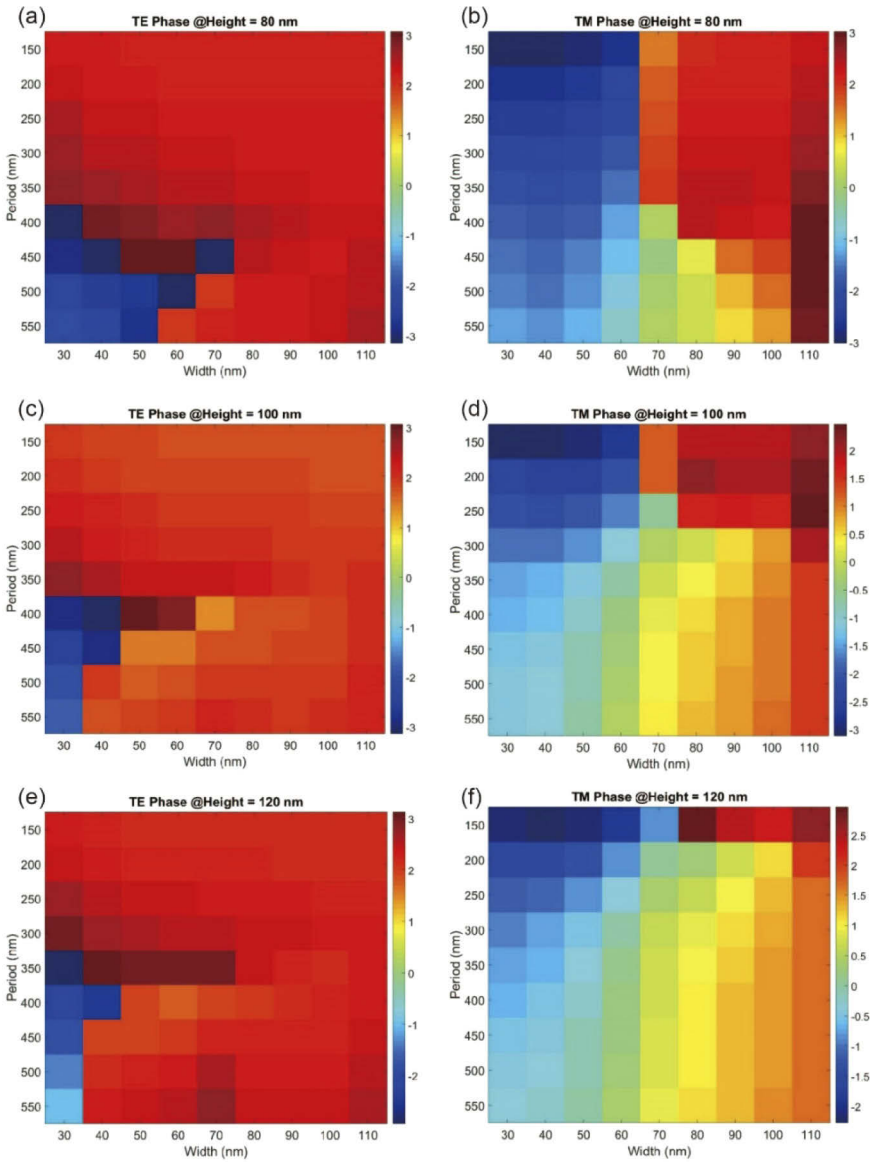

Fig. 1. (a), (c), (e): Phase maps of TE-polarized light at different heights; and (b), (d), (f): Phase maps of TM-polarized light at different heights.

Optics EXPRESS

HCG consisting of 300 nm period high-index stripes was the best compromise for achieving high transmission while maintaining full phase control; in fact, the phase response is achieved by rotating the optical axis of the grating [19]. It should be noted that this full 2π phase control is the comprehensive effect of both PB-phase and resonant phase supported by the HCG, which allows to achieve thinner structures.

A high efficiency OAM generator was designed accordingly and fabricated to verify the optical performance. The general features of an OAM generator based on geometrical phase are as follows: a left-circularly polarized input beam $E_{in} = E_0 \times (1,\ i)$ can be turned into a right-circular output beam $E_{out} = E_0 \exp(i2\alpha(x,\ y)) \times (1, -i)$, where $\alpha(x,\ y)$ is the orientation angle of the optical axis of each unit cell. If the azimuthal variation of the angle α follows the relation of $\alpha = q\varphi + \alpha_0$, the output wavefront then possesses $2|q|$ interwined helical surfaces carrying an OAM of $l = |2q\hbar|$, resulting in a topological singularity along the propagation axis [38–41]. Such beams are central to the field of singular optics, being a novel tool for manipulating the spin as well as the orientation of trapped objects [42,43]; additionally, such helical modes can be produced with our HCG metasurface. For the special instance of $q = 0.5$ and the incident light being left-circularly polarized, the output light is right-circularly polarized with an OAM per photon of $2\hbar$ (Fig. 2a).

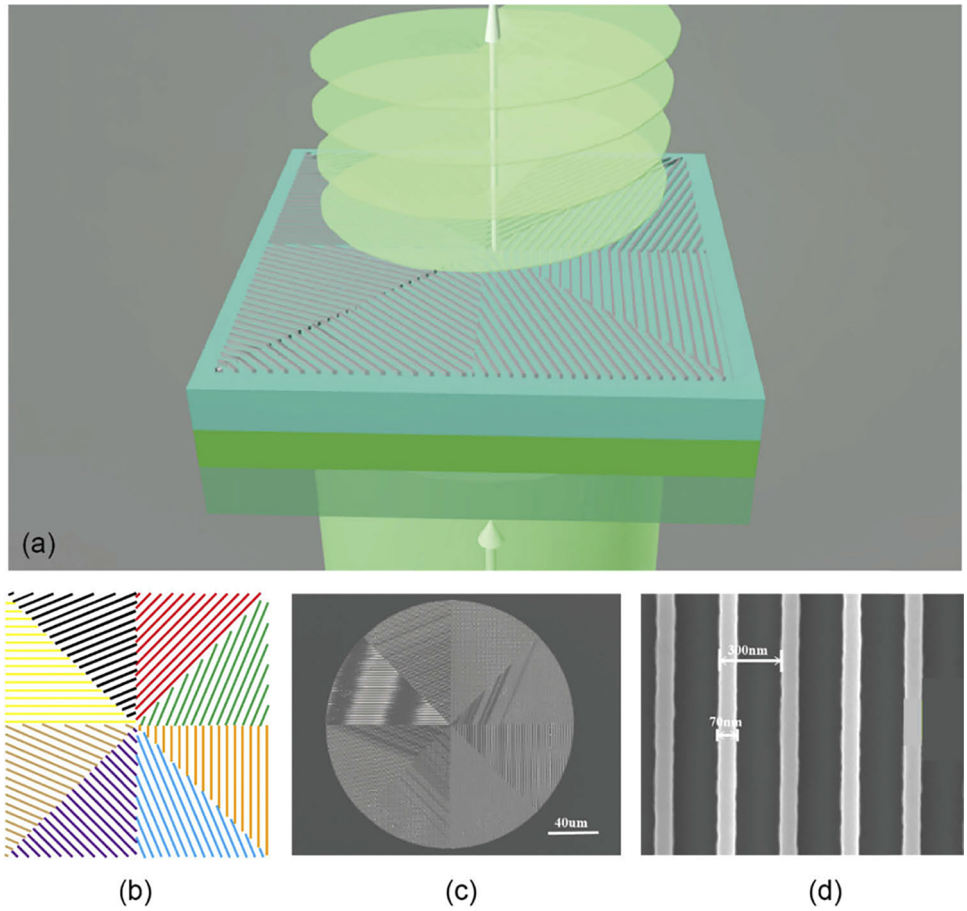

Fig. 2. (a) Schematic of the c-Si based HCG OAM generating metasurface. (b) Illustration of the HCG design with $|l| = 1$. (c) SEM micrograph of the complete metasurface and (d) its details.

Optics EXPRESS

The schematic arrangement of the OAM generator with $q = 0.5(|l| = 1)$ is shown in Fig. 2(b). This structure is then fabricated by electron beam lithography following the process. Figures 2(c) and 2(d) show SEM micrographs of the completed metasurface.

3. Methods

3.1. Sample fabrication

Before fabricating the transmissive metasurface, a thin c-Si layer is firstly transferred onto a quartz layer referred to Ref. [32] as a silicon-on-glass (SOG) wafer. Then the SOG sample is spin-coated with 400 nm ZEP520A as the electron beam resist; meanwhile, a 50 nm aluminum layer is thermal evaporated on the backside of the quartz to serve as the charge dissipation layer. The pattern is then exposed with electron beam lithography (EBL, Raith Vistec EBPG-5000 plus ES) at 100 keV. The exposed sample is then immersed into tetramethylammonium hydroxide (TMAH) to remove the aluminum layer, while the resist is developed with Xylene. Finally, the metasurface is finished after using inductively coupled plasma (ICP, Oxford Instruments) to etch 100 nm c-Si.

3.2. Measurement setup

The configuration of the Mach-Zehnder interferometer used to capture the output light intensity distribution is shown in Fig. 3(a). A cw laser beam (532 nm) is expanded and collimated by lenses L1 and L2 prior to being separated by a 50/50 beam splitter (BS). Half of the light (lower arm of the interferometer) passes through a quarter waveplate (QWP) to produce a left-circularly polarized (LCP) light; an objective lens (Obj1) then focuses the LCP beam onto the sample with a spot diameter of ~50 μm. The vortex beam created by the sample is re-collimated by another objective lens (Obj2) and passes through a QWP and a linear polarizer (LP) in cross-polarization with respect to QWP1 to eliminate the non-converted light. The reference beam propagates in the upper arm through a half waveplate (HWP) to acquire the same phase difference as in the lower arm. The interference pattern of the two beams occurring at the BS is finally captured by a CCD (D).

3.3. Numerical simulation method

To study the HCG structures and the performances of vortex beams, we used commercially available finite difference time-domain simulation software package (Lumerical FDTD). The 3D simulation was performed with periodic boundary conditions for HCG optimization, and with perfect matched layer (PML) boundary conditions for the OAM generators. The “Si (Silicon) - Palik” is chosen as the material of crystalline silicon. To balance the computational time and accuracy of the simulation, the mesh accuracy is chosen to be “4” in the software.

Optics EXPRESS

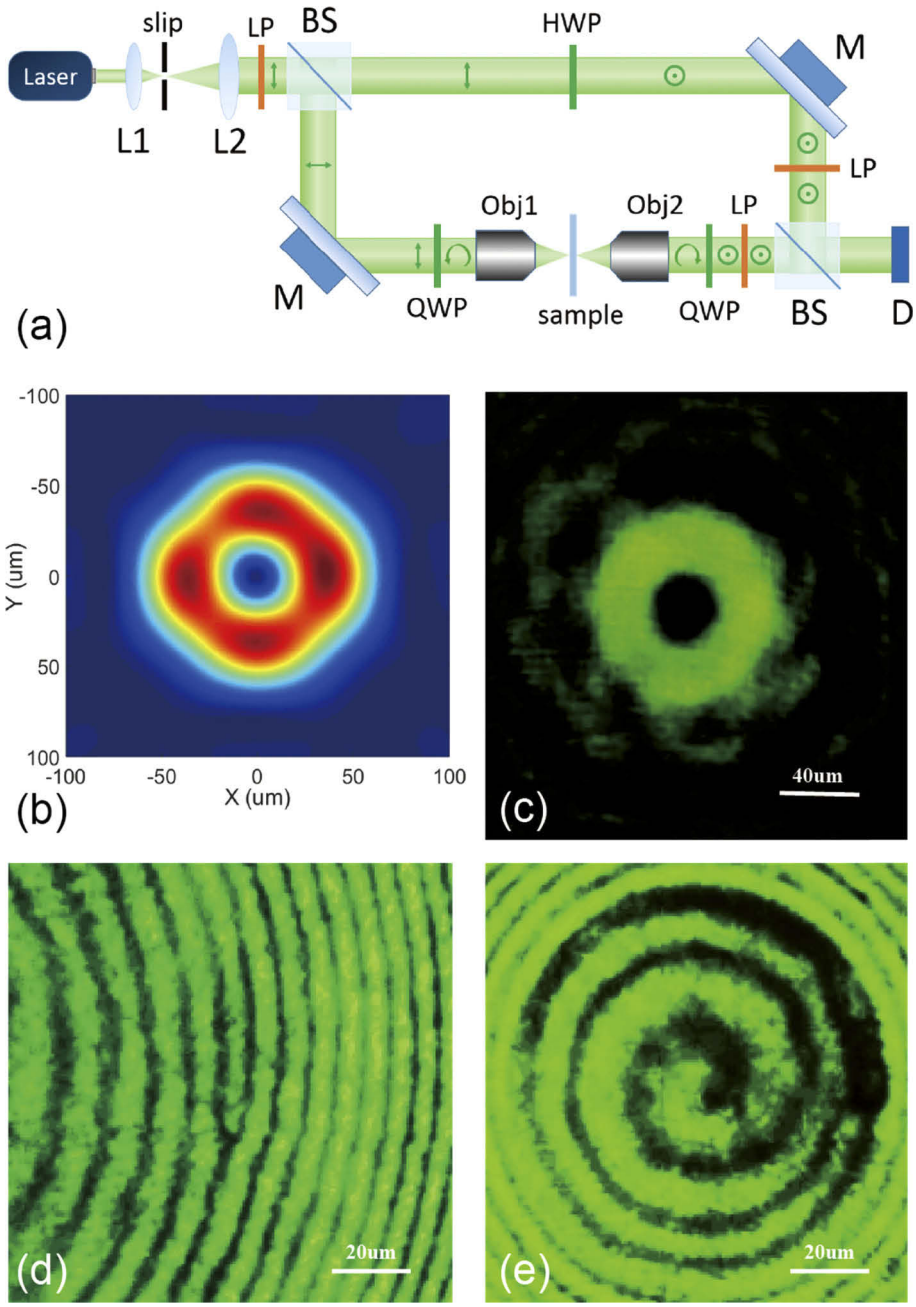

Fig. 3. (a) Configuration of the Mach-Zehnder interferometer used to capture the output light intensity distribution. (b) and (c) show the simulated and experimental vortex light intensity distribution with $|l| = 1$ generated by the OAM metasurface, respectively. We ensured a like-for-like comparison between simulation and measurement by modelling a segmented metasurface, as shown in Figs. 2b, c. (d) and (e) show the interference patterns obtained with a tilted reference beam (pitch-fork pattern) and a collinear reference beam (one-arm spiral) using the setup of Fig. 3a.

Optics EXPRESS

4. Measurement results

The intensity distribution of the output beam with $|l| = 1$ has a ring profile, as expected for a vortex beam. We use a Mach-Zehnder interferometer (Fig. 3a) to investigate the detailed phase singularities of the beam and to observe the expected pitch-fork and spiral beam patterns. The quality of the resulting figures highlights the high phase fidelity achieved with our metasurface.

The absolute efficiency is then defined as the amount of light converted into a helical mode divided by the incident light. We measure an experimental value of 63% efficiency at the operating wavelength of 532 nm, which is as high as a comparable TiO_2 nanofin metasurface of 600 nm thickness (reported to be 60% in [44]). As an added bonus, and as shown in Fig. 3(c), the quality of our OAM beam is even better than in our previous work on organic vortex laser metasurfaces [45].

5. Fabrication tolerances of thin HCGs

In order to assess fabrication tolerances, we simulated the fidelity one would expect from a typical nanoimprint process. To this end, we considered that an ideal beam with topological charge of $|l| = 1$ has a Laguerre-Gaussian far-field intensity and a phase distribution as shown in Figs. 4(a) and 4(f), respectively. Figures 4(b)–4(e) then show the simulated beam profiles generated by the metasurface with printing resolutions of 60 nm, 70 nm, 80 nm and 90 nm with Figs. 4(g)–4(j) their corresponding in-plane phase distributions, respectively. We assume that a higher resolution than 60 nm yields the same optical performance as the original design, which becomes apparent when comparing Figs. 3(b) and 3(b); Fig. 3(b) is the theoretical beamshape expected for a segmented metasurface, while Fig. 3(b) is the shape expected for an experiment with 60 nm resolution. The two are basically indistinguishable. We note that the performance both in terms of beam shape and phase distribution then degrades with decreasing printing resolution. To quantify the fidelity of the optical performance, we use the following correlation function [46]:

$$F = \frac{\left|\int A_0^*(x,\ y)A_t(x,\ y)dxdy\right|^2}{\int |A_0(x,\ y)|^2 dxdy \int |A_t(x,\ y)|^2 dxdy} \tag{1}$$

where A_t (x, y) and A_0 (x, y) are the complex amplitudes of the ideal and the degraded patterns, respectively. We take Figs. 4(a) and 4(f) as the target intensity and phase, and the fidelity value F of the respective profiles is illustrated in Fig. 4(k) for the different printing resolutions. The highest fidelity we observe is $F = 0.9625$, with the deviation from unity due to the segmented phase sections; we note that the simulated and the experimental structures for a resolution = 60 nm achieve identical fidelity values. The value of F then drops rapidly with decreasing spatial resolution.

An additional aspect is that the resolution achieved in the nanoimprint process directly impacts on the aspect ratio of the individual features. Therefore, poor lithographic transfer will not allow making high aspect ratio pillars as required for making nanofin structures. To study this aspect, we also simulate the height versus fidelity of the same $|l| = 1$ patterned metasurface, this time using the best possible c-Si nanofins with heights ranging from 100 nm to 500 nm designed by the method in [37] (See Table 1 for detailed geometric parameters). The corresponding simulated output beam profile is shown in Figs. 5(a)–5(e) and Figs. 5(f)–5(j), respectively. It shows that the optimum OAM property, with a fidelity $F = 0.9513$, is obtained when the height of the nanofins reaches 500 nm. However, this aspect ratio (10:1) cannot be replicated with high accuracy using a nanoimprint process. In contrast, the ultra-thin HCG process introduced here only requires low aspect ratio structures and supports high OAM performance which can be readily replicated using nanoimprint lithography.

Optics EXPRESS

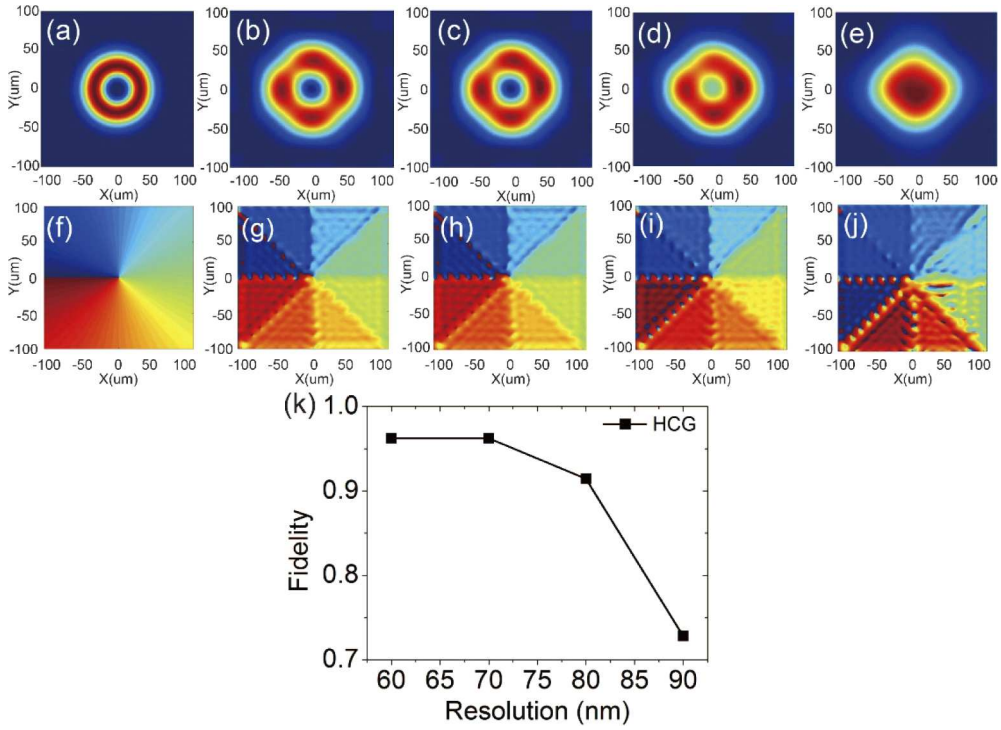

Fig. 4. (a) Ideal intensity distribution of a Laguerre-Gaussian beam with a topological charge of $|l| = 1$. (b) – (e) Far-field intensity distribution generated by the nanoimprinted c-Si HCG OAM generators with printing resolutions of 60 nm, 70 nm, 80 nm and 90 nm, respectively. (f) – (j) Corresponding phase distributions of (a) – (e). (k) Fidelity value for different printing resolutions.

Table 1. Geometric parameters of the nanofins used in this study

height (nm)	length (nm)	width (nm)	unit cell size (nm)	aspect ratio
100	100	20	160	5:1
200	105	78	110	2.6:1
300	135	36	142	8.3:1
400	147	43	163	9.3:1
500	160	50	220	10:1

Optics EXPRESS

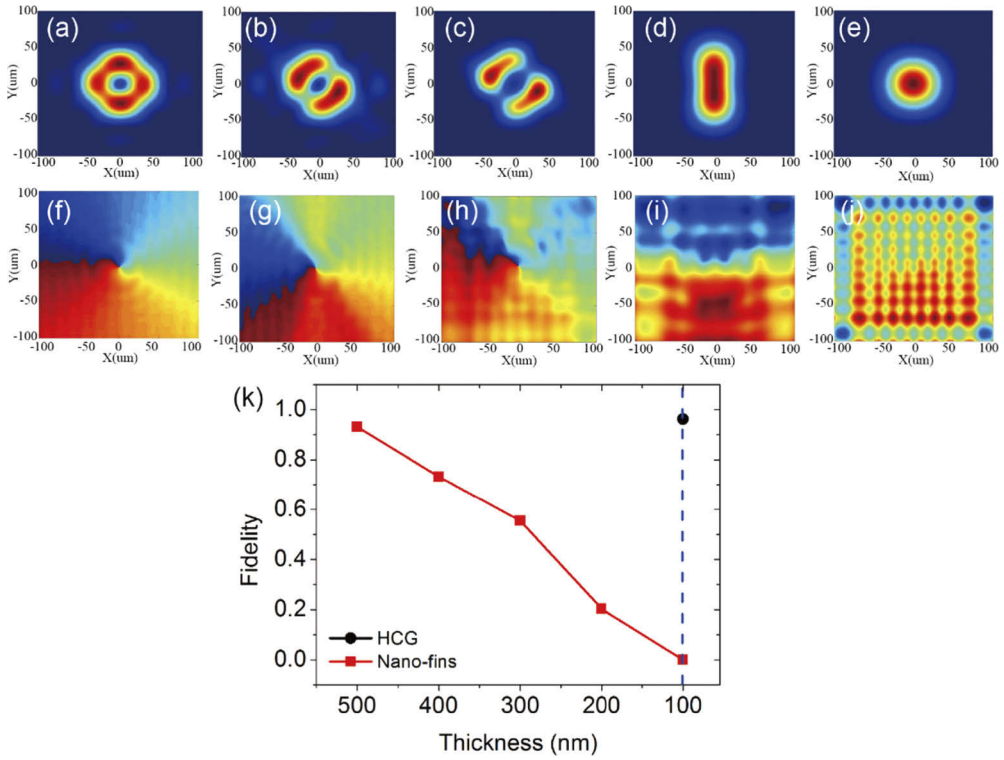

Fig. 5. (a) – (e) Far-field intensity distribution obtained by metasurfaces consisting of c-Si nanofins with heights of 500, 400, 300, 200 and 100 nm, respectively. (f) – (j) Corresponding phase distributions of (a) – (e). (k) Fidelity value indicating the optical performance of metasurfaces composed of nanofins with different heights. The blue dashed line shows that our HCG metasurface has a much better optical performance than a comparable nanofin metasurface for a thickness of 100 nm.

6. Conclusion

In summary, we have shown that highly transmissive metasurfaces that generate high fidelity vortex beams for operation at 532 nm can be generated in a crystalline silicon thin film with a thickness as low as 100 nm. Despite the very low thickness, our HCG design affords full 2π phase control for circularly polarized incident light. The experimentally measured efficiency is 63%, which is determined from the fraction of light being converted into the helical mode and taking absorption and reflection losses into account. We note that this efficiency is higher than that of comparable metasurface structures realised in TiO2. Furthermore, we illustrate by modelling that the thin HCG design introduced here is much more robust to fabrication errors than a comparable high aspect ratio nanofin design. We believe that our thin film approach is capable of simplifying metasurface mass-manufacture and that it will open up this research area to real applications such as ultra-thin functional optical elements for quantum information processing or optical focusing and complex beam shaping.

Funding

National Key R&D Program of China (2016YFA0301300); National Natural Science Foundation of China (11534017, 11704421, 11761131001, 91750207); The Key R&D Program of Guangdong Province (2018B030329001, 2019B010152001); Guangzhou Science and Technology

Optics EXPRESS

Program key projects (201607010044); Fundamental Research Funds for the Central Universities; Engineering and Physical Sciences Research Council (EP/P030017/1); Royal Society (Wolfson Research Merit Award Scheme).

Disclosures

The authors declare no conflicts of interest.

References

1. J. B. Pendry, D. Schurig, and D. R. Smith, "Controlling Electromagnetic Fields," Science **312**(5781), 1780–1782 (2006).
2. U. Leonhardt, "Optical Conformal Mapping," Science **312**(5781), 1777–1780 (2006).
3. W. Cai and V. Shalaev, *Optical Metamaterials: Fundamentals and Applications*, (Springer, 2009).
4. N. Engheta and R. W. Ziolkowski, *Metamaterials: Physics and Engineering Explorations* (Wiley-IEEE, 2006).
5. N. I. Zheludev and Y. S. Kivshar, "From metamaterials to metadevices," Nat. Mater. **11**(11), 917–924 (2012).
6. N. Yu, P. Genevet, M. A. Kats, F. Aieta, J.-P. Tetienne, F. Capasso, and Z. Gaburro, "Light Propagation with Phase Discontinuities: Generalized Laws of Reflection and Refraction," Science **334**(6054), 333–337 (2011).
7. L. Liu, X. Zhang, M. Kenney, X. Su, N. Xu, C. Ouyang, Y. Shi, J. Han, W. Zhang, and S. Zhang, "Broadband Metasurfaces with Simultaneous Control of Phase and Amplitude," Adv. Mater. **26**(29), 5031–5036 (2014).
8. S. Kruk, B. Hopkins, I. I. Kravchenko, A. Miroshnichenko, D. N. Neshev, and Y. S. Kivshar, "Invited Article: Broadband highly efficient dielectric metadevices for polarization control," APL Photonics **1**(3), 030801 (2016).
9. P. R. West, S. Ishii, G. V. Naik, N. K. Emani, V. M. Shalaev, and A. Boltasseva, "Searching for better plasmonic materials," Laser Photonics Rev. **4**(6), 795–808 (2010).
10. J. Lin, J. P. B. Mueller, Q. Wang, G. Yuan, N. Antoniou, X.-C. Yuan, and F. Capasso, "Polarization-Controlled Tunable Directional Coupling of Surface Plasmon Polaritons," Science **340**(6130), 331–334 (2013).
11. F. Lu, F. G. Sedgwick, V. Karagodsky, C. Chase, and C. J. Chang-Hasnain, "Planar high-numerical-aperture low-loss focusing reflectors and lenses using subwavelength high contrast gratings," Opt. Express **18**(12), 12606–12614 (2010).
12. S. Wang, P. C. Wu, V.-C. Su, Y.-C. Lai, C. Hung Chu, J.-W. Chen, S.-H. Lu, J. Chen, B. Xu, C.-H. Kuan, T. Li, S. Zhu, and D. P. Tsai, "Broadband achromatic optical metasurface devices," Nat. Commun. **8**(1), 187 (2017).
13. L. Huang, X. Chen, H. Mühlenbernd, H. Zhang, S. Chen, B. Bai, Q. Tan, G. Jin, K.-W. Cheah, C.-W. Qiu, J. Li, T. Zentgraf, and S. Zhang, "Three-dimensional optical holography using a plasmonic metasurface," Nat. Commun. **4**(1), 2808 (2013).
14. X. Ni, A. V. Kildishev, and V. M. Shalaev, "Metasurface holograms for visible light," Nat. Commun. **4**(1), 2807 (2013).
15. G. Zheng, H. Mühlenbernd, M. Kenney, G. Li, T. Zentgraf, and S. Zhang, "Metasurface holograms reaching 80% efficiency," Nat. Nanotechnol. **10**(4), 308–312 (2015).
16. W. T. Chen, K.-Y. Yang, C.-M. Wang, Y.-W. Huang, G. Sun, I. D. Chiang, C. Y. Liao, W.-L. Hsu, H. T. Lin, S. Sun, L. Zhou, A. Q. Liu, and D. P. Tsai, "High-Efficiency Broadband Meta-Hologram with Polarization-Controlled Dual Images," Nano Lett. **14**(1), 225–230 (2014).
17. R. Paniagua-Domínguez, Y. F. Yu, E. Khaidarov, S. Choi, V. Leong, R. M. Bakker, X. Liang, Y. H. Fu, V. Valuckas, L. A. Krivitsky, and A. I. Kuznetsov, "A Metalens with a Near-Unity Numerical Aperture," Nano Lett. **18**(3), 2124–2132 (2018).
18. A. Arbabi, Y. Horie, A. J. Ball, M. Bagheri, and A. Faraon, "Subwavelength-thick lenses with high numerical apertures and large efficiency based on high-contrast transmitarrays," Nat. Commun. **6**(1), 7069 (2015).
19. D. Lin, P. Fan, E. Hasman, and M. L. Brongersma, "Dielectric gradient metasurface optical elements," Science **345**(6194), 298–302 (2014).
20. C. J. Chang-Hasnain, "High-contrast gratings as a new platform for integrated optoelectronics," Semicond. Sci. Technol. **26**(1), 014043 (2011).
21. A. She, S. Zhang, S. Shian, D. R. Clarke, and F. Capasso, "Large area metalenses: design, characterization, and mass manufacturing," Opt. Express **26**(2), 1573–1585 (2018).
22. Z. Xie, T. Lei, F. Li, H. Qiu, Z. Zhang, H. Wang, C. Min, L. Du, Z. Li, and X. Yuan, "Ultra-broadband on-chip twisted light emitter for optical communications," Light: Sci. Appl. **7**(4), 18001 (2018).
23. Q.-T. Li, F. Dong, B. Wang, F. Gan, J. Chen, Z. Song, L. Xu, W. Chu, Y.-F. Xiao, Q. Gong, and Y. Li, "Polarization-independent and high-efficiency dielectric metasurfaces for visible light," Opt. Express **24**(15), 16309–16319 (2016).
24. M. Khorasaninejad, A. Ambrosio, P. Kanhaiya, and F. Capasso, "Broadband and chiral binary dielectric meta-holograms," Sci. Adv. **2**(5), e1501258 (2016).
25. B. Wang, F. Dong, Q.-T. Li, D. Yang, C. Sun, J. Chen, Z. Song, L. Xu, W. Chu, Y.-F. Xiao, Q. Gong, and Y. Li, "Visible-Frequency Dielectric Metasurfaces for Multiwavelength Achromatic and Highly Dispersive Holograms," Nano Lett. **16**(8), 5235–5240 (2016).

Optics EXPRESS

26. K. E. Chong, L. Wang, I. Staude, A. R. James, J. Dominguez, S. Liu, G. S. Subramania, M. Decker, D. N. Neshev, I. Brener, and Y. S. Kivshar, "Efficient Polarization-Insensitive Complex Wavefront Control Using Huygens' Metasurfaces Based on Dielectric Resonant Meta-atoms," ACS Photonics **3**(4), 514–519 (2016).
27. Y. Yang, W. Wang, A. Boulesbaa, I. I. Kravchenko, D. P. Briggs, A. Puretzky, D. Geohegan, and J. Valentine, "Nonlinear Fano-Resonant Dielectric Metasurfaces," Nano Lett. **15**(11), 7388–7393 (2015).
28. M. Khorasaninejad, W. T. Chen, R. C. Devlin, J. Oh, A. Y. Zhu, and F. Capasso, "Metalenses at visible wavelengths: Diffraction-limited focusing and subwavelength resolution imaging," Science **352**(6290), 1190–1194 (2016).
29. W. T. Chen, A. Y. Zhu, M. Khorasaninejad, Z. Shi, V. Sanjeev, and F. Capasso, "Immersion Meta-Lenses at Visible Wavelengths for Nanoscale Imaging," Nano Lett. **17**(5), 3188–3194 (2017).
30. M. Khorasaninejad, Z. Shi, A. Y. Zhu, W. T. Chen, V. Sanjeev, A. Zaidi, and F. Capasso, "Achromatic Metalens over 60 nm Bandwidth in the Visible and Metalens with Reverse Chromatic Dispersion," Nano Lett. **17**(3), 1819–1824 (2017).
31. R. C. Devlin, M. Khorasaninejad, W. T. Chen, J. Oh, and F. Capasso, "Broadband high-efficiency dielectric metasurfaces for the visible spectrum," Proc. Natl. Acad. Sci. **113**(38), 10473–10478 (2016).
32. Z. Zhou, J. Li, R. Su, B. Yao, H. Fang, K. Li, L. Zhou, J. Liu, D. Stellinga, C. P. Reardon, T. F. Krauss, and X. Wang, "Efficient Silicon Metasurfaces for Visible Light," ACS Photonics **4**(3), 544–551 (2017).
33. D. Sell, J. Yang, S. Doshay, K. Zhang, and J. A. Fan, "Visible Light Metasurfaces Based on Single-Crystal Silicon," ACS Photonics **3**(10), 1919–1925 (2016).
34. D. Sell, J. Yang, S. Doshay, R. Yang, and J. A. Fan, "Large-Angle, Multifunctional Metagratings Based on Freeform Multimode Geometries," Nano Lett. **17**(6), 3752–3757 (2017).
35. A. B. Klemm, D. Stellinga, E. R. Martins, L. Lewis, G. Huyet, L. O'Faolain, and T. F. Krauss, "Experimental high numerical aperture focusing with high contrast gratings," Opt. Lett. **38**(17), 3410–3413 (2013).
36. G. Tkachenko, D. Stellinga, A. Ruskuc, M. Chen, K. Dholakia, and T. F. Krauss, "Optical trapping with planar silicon metalenses," Opt. Lett. **43**(14), 3224–3227 (2018).
37. H. Liang, Q. Lin, X. Xie, Q. Sun, Y. Wang, L. Zhou, L. Liu, X. Yu, J. Zhou, T. F. Krauss, and J. Li, "Ultrahigh Numerical Aperture Metalens at Visible Wavelengths," Nano Lett. **18**(7), 4460–4466 (2018).
38. A. Mair, A. Vaziri, G. Weihs, and A. Zeilinger, "Entanglement of the orbital angular momentum states of photons," Nature **412**(6844), 313–316 (2001).
39. H. Ren, G. Briere, X. Fang, P. Ni, R. Sawant, S. Héron, S. Chenot, S. Vézian, B. Damilano, V. Brändli, S. A. Maier, and P. Genevet, "Metasurface orbital angular momentum holography," Nat. Commun. **10**(1), 2986 (2019).
40. R. C. Devlin, A. Ambrosio, N. A. Rubin, J. P. B. Mueller, and F. Capasso, "Arbitrary spin-to–orbital angular momentum conversion of light," Science **358**(6365), 896–901 (2017).
41. J. Wang, Z. Shao, Y. Wen, X. Qiu, Y. Chen, Y. Zhang, S. Yu, and L. Chen, "All-dielectric metasurface grating for on-chip multi-channel orital angular momentum generation and detection," Opt. Express **27**(13), 18794–18802 (2019).
42. M. Padgett and R. Bowman, "Tweezers with a twist," Nat. Photonics **5**(6), 343–348 (2011).
43. M. E. J. Friese, J. Enger, H. Rubinsztein-Dunlop, and N. R. Heckenberg, "Optical angular-momentum transfer to trapped absorbing particles," Phys. Rev. A **54**(2), 1593–1596 (1996).
44. R. C. Devlin, A. Ambrosio, D. Wintz, S. L. Oscurato, A. Y. Zhu, M. Khorasaninejad, J. Oh, P. Maddalena, and F. Capasso, "Spin-to-orbital angular momentum conversion in dielectric metasurfaces," Opt. Express **25**(1), 377–393 (2017).
45. D. Stellinga, M. E. Pietrzyk, J. M. E. Glackin, Y. Wang, A. K. Bansal, G. A. Turnbull, K. Dholakia, I. D. W. Samuel, and T. F. Krauss, "An Organic Vortex Laser," ACS Nano **12**(3), 2389–2394 (2018).
46. A. Liu, C.-L. Zou, X. Ren, Q. Wang, and G.-C. Guo, "On-chip generation and control of the vortex beam," Appl. Phys. Lett. **108**(18), 181103 (2016).